Correlating results from high resolution EBSD with TEM- and ECCI-based dislocation microscopy: Approaching single dislocation sensitivity via noise reduction

T.J. Ruggles[a,b,*], Y.S.J. Yoo[c], B.E. Dunlap[d], M.A. Crimp[d], J. Kacher[c]

[a]*National Institute of Aerospace, Hampton, VA, USA*
[b]*Sandia National Laboratories, Albuquerque, NM, USA*
[c]*Georgia Institute of Technology, Atlanta, GA, USA*
[d]*Michigan State University, East Lansing, MI, USA*

Abstract

High resolution electron backscatter diffraction (HREBSD), an SEM-based diffraction technique, may be used to measure the lattice distortion of a crystalline material and to infer the geometrically necessary dislocation content. Uncertainty in the image correlation process used to compare diffraction patterns leads to an uneven distribution of measurement noise in terms of the lattice distortion, which results in erroneous identification of dislocation type and density. This work presents a method of reducing noise in HREBSD dislocation measurements by removing the effect of the most problematic components of the measured distortion. The method is then validated by comparing with TEM analysis of dislocation pile-ups near a twin boundary in austenitic stainless steel and with ECCI analysis near a nano-indentation on a tantalum oligocrystal. The HREBSD dislocation microscopy technique is able to resolve individual dislocations visible in TEM and ECCI and correctly identify their Burgers vectors.

Keywords: HREBSD, dislocation microscopy, TEM, ECCI

1. Introduction

The mechanical behavior of ductile, crystalline materials is dictated largely by the collective motion and accumulation of dislocations. A fundamental understanding of how the dislocation state in a material evolves as a function of applied loading conditions is essential to understanding basic material behavior such as work hardening, fatigue damage accumulation, and creep. Detecting and mapping dislocation structures has historically been the domain of transmission electron microscopy (TEM), where individual dislocations and dislocation networks can be resolved and characterized in terms of their density, slip plane, line direction, and Burgers vector. However, TEM is limited in both the maximum characterizable area, which is on the order of tens to hundreds of microns, and maximum sample thickness, requiring destructive sample preparation and limiting in situ deformation investigations to thin films. For these reasons, TEM-based dislocation characterization excels at understanding local dislocation phenomena, but not at mesoscale mapping of dislocation structures and their evolution under applied loading conditions, motivating the search for additional avenues for dislocation characterization.

Electron channeling contrast imaging (ECCI) is a scanning electron microscope (SEM)-based technique that offers an alternative to TEM for the direct imaging and characterization of dislocation structures [1, 2]. While ECCI offers significantly weaker contrast, is often more limited in tilt range, and is more difficult to carry out than TEM, particularly if the instrument at hand does not have selected area electron channeling capabilities, it offers the ability to examine the dislocation structures in the near surface region of bulk samples. Thus, ECCI is not limited to thin foils and destructive sample preparation, allowing ECCI to be carried out on very large areas of interest. Furthermore, ECCI allows TEM style contrast analysis to determine Burgers vectors and dislocation line direction [3–5].

Electron backscatter diffraction (EBSD) based dislocation microscopy provides another method for measuring dislocation content in an SEM. Conventional EBSD software/hardware set-ups determine the local crystallographic orientation of a material with about 0.1-0.5^{o} resolution [6, 7]. This orientation information may be used

*Corresponding author. Tel.: +1 505 844 7017
Email address: truggle@sandia.gov (T.J. Ruggles)

to infer the geometrically necessary dislocation (GND) content of the material via the Nye-Kröner-Bilby relationship in a continuum sense [8–11]. High resolution EBSD (HREBSD), a means of extracting relative elastic strain and misorientation between patterns to a much greater accuracy (around 0.006^{o} for typical equipment and ideal conditions [12]) has further improved the resolution and accuracy of EBSD dislocation microscopy [13–24]. HREBSD dislocation microscopy has simple, relatively non-destructive sample preparation like ECCI, but it has the advantage of being largely automated. Using ECCI to identify dislocations requires manual tilt and rotation procedures, which are not typically automated. Because of long exposure times for diffraction patterns and computationally intensive image processing, HREBSD can take more instrument time and analysis time than ECCI, but it requires far less user input. Because of the necessity of calculating numerical derivatives for dislocation analysis, HREBSD has inferior spatial resolution compared to ECCI. However, because it is formulated for continuum analysis, HREBSD is superior at analyzing dislocation content at large length scales and higher dislocation densities compared to ECCI. HREBSD dislocation microscopy also has difficulty sorting out dislocation densities of individual Burgers vector/line direction combinations because relating the continuum dislocation density tensor to individual dislocation densities is an underconstrained problem. When it may be assumed that only one dislocation type is present in an area (for example at small length scales where only a single dislocation or pile-up strongly influences the lattice distortion gradients), and that dislocation type's line direction is not parallel to the surface, the exact dislocation type may be recovered [19]. Because of these contrasting, but overlapping capabilities, ECCI and HREBSD maybe thought of as complementary techniques.

The resolution of HREBSD dislocation microscopy has been steadily improving. Recently, studies have favorably compared the results with ECCI, but these studies stopped short of identifying individual dislocations with both methods [25–27]. Prior work by the authors has shown qualitative agreement between TEM and HREBSD dislocation measurements [28]. Both the deformation resolution and the spatial resolution of HREBSD limit its utility in detecting individual dislocations. Several efforts are underway that will favorably impact the spatial resolution of EBSD, including transmission Kikuchi diffraction (TKD) [29–31], direct electron detectors [32] and improved EBSD pattern simulation (which allows the use of lower accelerating voltage) [33–35]. TKD in particular has been shown to accurately detect dislocation fields [36] and, when using the cross-correlation-based approach of HREBSD, has been used to accurately measure the strain fields around individual dislocations in tungsten [37], though this comes at the expense of thinning the sample to electron transparency. Because of continued improvements in EBSD/TKD detector technology, such as the recent advent of complementary metal-oxide semiconductor (CMOS)-based detectors associated with an order of magnitude increase in the rate of high resolution pattern collection, HREBSD and HRTKD are expected to see increasingly widespread use.

This paper presents a method for improving the geometrically necessary dislocation density resolution of HREBSD dislocation microscopy by reducing the effects of noise in the process. This method takes advantage of the uneven noise distributed between components of the deformation gradient tensor when measured via HREBSD [38, 39]. These noisy deformation components may be isolated as individual terms of the measured deformation gradient when transformed into the reference frame of the diffraction detector. When applied, this noise reduction operation allows HREBSD to identify individual dislocations (or clumps of a few similar dislocations if they are close together) by their Burgers vectors and in some cases their line direction as well. This capability is confirmed by comparing HREBSD results to dislocation analysis performed by TEM on two dislocation pile-ups in an austenitic 302 stainless steel sample. The method is also applied to an HREBSD scan from a previous study [27] that was taken around a nanoindent in tantalum that was concurrently characterized with ECCI. The implications of this work on the limitations and capabilities of HREBSD dislocation microscopy are discussed in detail in the conclusion.

2. Background

HREBSD is a method where image correlation is performed between a reference and a test EBSD pattern to determine their relative deformation in the plane of the diffraction detector. This deformation may then be related via the geometry of diffraction to the deformation between the lattices where each pattern originated. Although more complex methods of image correlation have been developed recently for HREBSD [40–43] this paper will focus on cross-correlation, which is the standard method used with HREBSD because of its computational speed and simplicity. With cross-correlation HREBSD (sometimes abbreviated CCEBSD), the two patterns are divided

into a number of overlapping regions of interest (ROIs) and cross-correlation is performed to measure a shift between the patterns for each ROI. The relationship between a measured shift, $\vec{q}$, and the desired 3D elastic deformation gradient between the patterns, $\mathbf{F}$, is diagrammed in Figure 1.

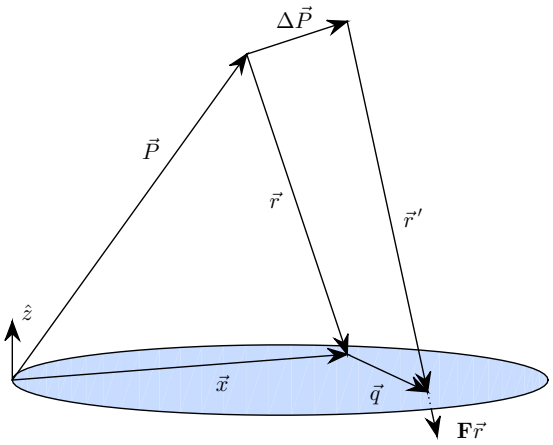

Figure 1: Illustration of the geometry of HREBSD relative to the detector used to collect the pattern (bottom).

The other terms in Figure 1 are $\vec{P}$, the location of the reference interaction volume relative to the EBSD detector (also called the pattern center), $\Delta\vec{P}$, the displacement vector between the test pattern's interaction volume and the reference pattern's, and $\vec{x}$, the location of the ROI's center. The vector $\vec{r}$ is defined as the vector between the reference pattern center and the ROI center, and $\vec{r}'$ is defined as the vector between the test pattern interaction volume and the shifted center of the ROI. Any change in the direction of $\vec{r}'$ relative to $\vec{r}$ is due to the deformation gradient between the patterns, i.e. $\vec{r}' \parallel \mathbf{F}\vec{r}$. The direction normal to the plane of the detector is $\hat{z}$. The relationship between the shift, the relative deformation gradient and the relevant geometric terms is encapsulated in Equation 1 (see [41] for the full derivation of this equation):

$$\vec{q} = \Delta\vec{P} + \mathbf{F}\vec{r}\frac{-(\vec{P}+\Delta\vec{P})\cdot\hat{z}}{\mathbf{F}\vec{r}\cdot\hat{z}} - \vec{r} \tag{1}$$

Equation 1 from at least four non-collinear ROIs form a system of equations that may be used to calculate eight degrees of freedom of $\mathbf{F}$. In practice, anywhere from 20 to 200 ROIs are used, with 50 being a typical value. The last, missing degree of freedom is approximately equal to the spherical strain component of $\mathbf{F}$ and cannot be recovered because of the projection of $\mathbf{F}\vec{r}$ onto the detector surface. This missing degree of freedom is typically recovered either by enforcing the traction free condition [44], or by recovering only the portion of the deformation gradient associated with deviatoric stress [45]. For typical detector resolutions and pristine patterns, the relative accuracy of this method is often quoted as 200 microstrain [12].

Naturally, uncertainty in $\vec{q}$ propagates as uncertainty in $\mathbf{F}$. However, it is less obvious that this uncertainty is not evenly distributed across all components of $\mathbf{F}$. In order to elucidate this relationship, it is convenient to substitute $(\vec{x}-\vec{P})$ for $\vec{r}$. Additionally, the substitution $\mathbf{F} = \mathbf{I}+\beta$ (β here is commonly referred to as the lattice distortion) is made so that each term has a similar magnitude:

$$\vec{q} = \vec{P} + \Delta\vec{P} + (\mathbf{I}+\beta)\vec{r}\frac{-(\vec{P}+\Delta\vec{P})\cdot\hat{z}}{(\mathbf{I}+\beta)\vec{r}\cdot\hat{z}} - \vec{x} \tag{2}$$

The derivatives of $\vec{q}$ with respect to the terms of β provide insight into how the different terms will have different sensitivity to error in $\vec{q}$. The derivatives are determined at the point where $\beta = \mathbf{0}$ and $\Delta\vec{P} = \vec{0}$ and in the reference frame where the z-axis is normal to the detector and the origin lies in the plane of the detector (i.e. $q_3 = x_3 = 0$) [38]:

$$\frac{dq_i}{d\beta_{jk}} = \begin{cases} 0 & i \neq j, j \neq 3 \\ x_k - P_k & i = j, k \neq 3 \\ -P_3 & i = j, k = 3 \\ \dfrac{(x_k - P_k)(x_i - P_i)}{P_3} & j = 3, k \neq 3 \\ P_i - x_i & j = k = 3 \end{cases} \tag{3}$$

where $i \in \{1,2\}$ and $j,k \in \{1,2,3\}$. From Equation 3, we see that to a first order approximation the β_{11}, β_{12}, β_{21} and β_{22} terms represent a linear deformation between the two patterns in the plane of the detector, β_{13} and β_{23} represent a translation, and β_{31} and β_{32} represent non-linear deformation between the patterns [41]. The term β_{33} represents a linear dilation in the pattern plane, and is therefore redundant with the linear transformation terms, which is why the traction free or deviatoric constraint is required in HREBSD. It is also important to note that individual terms have very different relationships with different components of the pattern center, $\vec{P}$. For example, the terms that approximate a linear shift, β_{13} and β_{23} are approximately independent of $(x_1 - P_1)$ and $(x_2 - P_2)$ and have a linear relationship with P_3, while the non-linear deformation terms β_{31} and β_{32} have a quadratic relationship with $(x_1 - P_1)$ and $(x_2 - P_2)$ and an inverse relationship with P_3.

While these derivatives are instructive, particularly with regards to how simple geometric factors like detector distance and ROI spacing can affect HREBSD results, the

relationship between uncertainty in individual terms of β, $\sigma(\beta_{ij})$, and uncertainty in measurement of $\vec{q}$ is more useful. Because β depends on the particular arrangement of a large number of ROIs used, it is difficult to obtain or interpret these results analytically, even with symbolic solvers. Instead, the relationship between uncertainty in $\vec{q}$ and uncertainty in β was determined via simple Monte Carlo simulations. A similar simulation was performed previously, but with no emphasis on individual terms of the deformation gradient [46]. In reality, measurement error in $\vec{q}$ stems from the resolution of the diffraction images and white noise in the pattern [47]. To simulate this, the shifts, $\vec{q}$, were drawn from a normal distribution, with a standard deviation of σ_q for both the x and y component. These randomly generated shifts were then inserted into Equation 1, a system of equations is created from all the shifts and β is calculated. Because there was no simulated lattice distortion, this β is entirely the propagated error. Repeating this process a large number of times allows the recovery of $\sigma(\beta_{ij})$. The N ROIs were arranged annularly about the center of the pattern with a radius of ρ. The pattern center was selected to be $\vec{P} = [0.5; 0.5; d]$, in units of fractions of the phosphor screen width. The expression d is referred to as the detector distance. The ninth degree of freedom of β was determined by setting the trace of β to 0, which is a linear approximation of the deviatoric constraint for cubic materials. Note that this simple Monte Carlo simulation requires no crystallographic information, and no simulation of either EBSD patterns or cross-correlation, because the shift error is simply drawn from a normal distribution. The parameters σ_q, ρ, d and N were varied over ranges relevant to HREBSD ($\sigma_q = 0.01$ to 1 pixel, $\rho = 15$ to 45% of the detector screen width, $d = 20$ to 100% of the detector screen width, and $N = 4$ to 100) and 10,000 simulations were performed to determine $\sigma(\beta_{ij})$ at each set of HREBSD parameters. From this data, the following relationships were determined empirically:

$$\sigma(\beta_{13}), \sigma(\beta_{23}) \approx \frac{\sqrt{2}}{d\sqrt{N}}\sigma_q \tag{4}$$

$$\sigma(\beta_{31}), \sigma(\beta_{32}) \approx \frac{2d}{\rho^2\sqrt{N}}\sigma_q \tag{5}$$

$$\sigma(\beta_{12}), \sigma(\beta_{21}) \approx \frac{\sqrt{2}}{\rho\sqrt{N}}\sigma_q \tag{6}$$

$$\sigma(\beta_{11}), \sigma(\beta_{22}) \approx \frac{1.05}{\rho\sqrt{N}}\sigma_q \tag{7}$$

$$\sigma(\beta_{33}) \approx \frac{0.67}{\rho\sqrt{N}}\sigma_q \tag{8}$$

The relationship between sensitivity and the geometric parameters d and ρ is supported by the derivatives of $\vec{q}$ with respect to the terms of β, where the detector distance, d, is analogous to P_3 and the ROI radius, ρ, is analogous to $\sqrt{(x_1 - P_1)^2 + (x_2 - P_2)^2}$. The inverse relationship with $\sqrt{N}$ is consistent with the central limit theorem. However, there are three important caveats to go along with Equations 4-8. The first is that the constants depend on the choice of constraint to recover the ninth degree of freedom. The second is that the inverse $\sqrt{N}$ relationship assumes that additional shifts are independent, meaning it should only hold as long as the ROIs are not overlapping. Finally, these relationships depend on the ROIs being annularly distributed about the pattern center, and any variation in that arrangement will lead to different results. Using these results and assuming typical geometric parameters ($\rho = 0.25$ and $d = 0.65$ in units of fractions of the detector width), the ratio of the noise in the most susceptible terms (β_{31} and β_{32}) to the least susceptible (β_{13} and β_{23}) is 9.6, almost an order of magnitude.

This model of the noise in different terms of β measured by HREBSD holds well with actual data from a piece of epitaxial silicon that was scanned in a previous work [39]. HREBSD was performed with each point in the scan as the reference pattern with its neighbor to the right as the test pattern (such as would be calculated to determine lattice distortion gradients). The material was assumed to be strain and defect free, so any measured deformation was assumed to be error due to random noise. The scan was taken at 20 kV with a beam current of 13 nA over a 60×60 micron area with a step size of 0.4 microns in a Helios^{TM} SEM. The patterns were collected with no binning on a Hikari Super^{TM} camera with no gain and an exposure time of 200 ms. The working distance was approximately 12 mm. A histogram of each term of β in the reference frame of the detector is shown in Figure 2a. For comparison, a similar histogram for data generated via Monte Carlo is shown in Figure 2b. For the simulation, no real distortion was simulated, only noise. The geometric parameters were selected to match the real data, $d = .65$, $\rho = 0.25$, and $N = 48$. The shift error, σ_q was fit empirically so that the data sets had the same magnitude, and was found to be 8.2% of a pixel. Because the real scan had overlapping ROIs, σ_q must be thought of as a fitting parameter, rather than an estimate of the actual uncertainty. Note the good agreement between the real data and the simulation.

While highly effective at modeling the relative noise of individual terms in HREBSD measurements of the deformation gradient, this model relies on the assumption

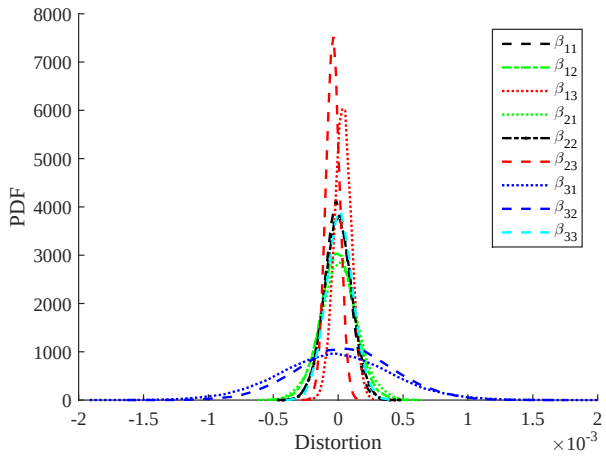

(a)

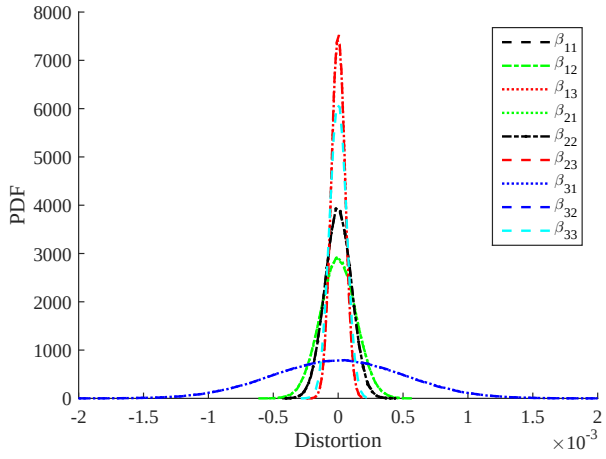

(b)

Figure 2: Histograms of the terms of β in the detector reference frame for (a) an epitaxial silicon sample where any measured distortion is assumed to be erroneous and (b) a Monte Carlo simulation where the measured shifts were random noise.

that noise in the shifts is uniform and random. This is not the case in reality. For example, pattern center error can result in offset type error [38]. The fact that β_{13} and β_{23} do not have a mean of 0, for example, suggests that there is some error in the calibration of the spacing between points in the scan, $\Delta\vec{P}$. Additionally, the signal to noise ratio of the pattern depends on the level of illumination, which varies across the surface of the detector, meaning that σ_q is not constant for all points on a pattern. Finally, shift error will also depend on the sharpness and complexity of the features in the ROI, which means that shift error will also be a function of crystal orientation. All of these effects are small or may be mitigated with good practice, and so their inclusion is not necessary to qualitatively match the experimental results in Figure 2a. Shift error will also strongly depend on ROI size, but it should have no effect on the relative error of different components.

Once the relative distortions between neighboring points in a scan is measured via HREBSD, they may be used to estimate the two orthogonal derivatives of the distortion on the surface of the material with the following equation:

$$\left.\frac{d\beta}{dx_i}\right|_{\vec{p}} = \frac{\beta^{\vec{p},\vec{p}+\Delta\vec{x}_i}}{L} \tag{9}$$

where $\vec{p}$ is a location on the surface of a scan, $\Delta\vec{x}_i$ is the vector between the first pattern and an adjacent pattern, L is the spacing between raster points and the magnitude of $\Delta\vec{x}_i$, and $\beta^{\vec{p},\vec{p}+\Delta\vec{x}_i}$ is the relative distortion between patterns at location $\vec{p}$ and $\vec{p}+\Delta\vec{x}_i$. These derivatives may be obtained by cross-correlating each pattern with its nearest neighbors or by cross-correlating each pattern with a single reference pattern per grain and then calculating the relative distortions. In this work, each relative distortion is calculated separately, using every point as a reference for its neighbors. Determining relative distortions in this way minimizes the need for remapping [40, 41, 45, 48], reduces noise in the calculation by not compounding the random error between two separate cross-correlations and eliminates any bias associated with reference pattern selection. The downside of performing individual cross-correlations for each derivative is that it is twice as computationally intensive as computationally intensive as the reference pattern method (without remapping) and does not recover relative strain and orientation information at a grain level.

These derivatives may be related to the geometrically necessary dislocation content of the material via the fundamental relation of continuum dislocation theory [49–51]:

$$\alpha = \nabla \times \beta \tag{10}$$

Nye's tensor, α, provides a concise representation of net dislocation density and type on a continuum level. Nye's tensor may then be related to dislocation densities on individual dislocation types[52]:

$$\alpha = \sum_{t=1}^{N} \rho^t \vec{b}^t \otimes \vec{\ell}^t \tag{11}$$

where ρ^t, $\vec{b}^t$, and $\vec{\ell}^t$, represent the dislocation density, Burgers vector and dislocation line vector of each dislocation type (indicated by t), respectively. A dislocation type is here defined as a unique combination of Burgers vector

and dislocation line vector. There are a finite number of possible Burgers vectors, but due to the nature of mixed character dislocations there can be an infinite number of unique dislocation line vectors. To make this problem more tractable, this analysis makes the assumption that all dislocation content may be modeled as a linear superposition of pure edge and pure screw dislocation densities. Under this assumption, an FCC material like the austenitic stainless steel in this study, has 6 screw dislocation types for each Burgers vector in the family $\langle 110 \rangle$ (this method cannot distinguish between screw dislocations with the same Burgers vector on different slip planes) and 12 edge dislocation types (one for each slip system with $\langle 110 \rangle$ a Burgers vector and a $\{111\}$ slip plane). For BCC materials there are four screw dislocation types (one for each Burgers vector in the family $\langle 111 \rangle$), but depending on what slip planes are considered, the number of edge dislocation systems can vary. For the tantalum used in this study, both the $\{110\}$ and $\{112\}$ slip planes were considered for a total of 24 edge dislocation systems. Assuming we have distortion derivatives in only two directions (because a numerical derivative normal to the surface would only be possible via sectioning), we can only determine 3 terms of α, α_{i3}. By assuming that the strain part of the distortion derivatives is small, Pantleon noted that an additional two terms (α_{12} and α_{21}) and a difference of terms ($\alpha_{11} - \alpha_{22}$) become available [53]. This means that if the dislocation densities of individual dislocation types are desired, Equation 11 becomes an under constrained problem with 18 unknowns and at best 6 constraints (at worst 3). These constraints are usually incorporated into an energy minimization problem:

$$\text{minimize} \sum_{t=1}^{N} |w^t \rho^t|, \text{ such that } \alpha = \sum_{t=1}^{N} \rho^t \vec{b}^t \otimes \vec{\ell}^t \quad (12)$$

where w^t is a weighting factor for each dislocation type that allows more energetically favorable dislocations to be better represented and only the known/estimated terms of α are used. In this study, weight factors are set to unity. Note that the inclusion of the energy minimization constraint is somewhat arbitrary, because there is no guarantee that the dislocations at a given point are not in some metastable state. When calculating total dislocation density, also known as bulk dislocation density, use of the energy minimization constraint represents a lower bound of the dislocation density. For FCC materials, the 6 constraints and the minimization have been shown to be effective at resolving all 18 dislocation types when they are present individually (such as at very low length scales, as in this study), except in specific pathological cases where the orientation of the crystal is such that these dislocations are near parallel to the sample surface [19]. When multiple dislocation systems are present or when more dislocation systems must be considered, such as in the case of HCP materials or BCC materials when $\{112\}$ and/or $\{123\}$ planes are also taken into account, interpretation of these results becomes more ambiguous.

Selection of a step size for an EBSD scan, the spacing between points probed with the SEM, has a strong influence on dislocation density measurements because this step size also serves as the step size for the numerical derivative of the lattice distortion (Equation 9). At larger step sizes, the effect of noise is much lower, but more of the dislocation content cancels out due to the length scale dependent definition of geometrically necessary dislocations [54–58]. For this reason, the step sizes in this study are very low, 30 nm for the stainless steel and 25 nm for the tantalum, in an attempt to detect the total dislocation content of the material. The Nye-Kröner-Bilby method presented here was originally intended for treatment of dislocation densities as continua. Here, however, this method will be applied at a length scale where the influence of individual dislocations will be discernible, and the continuum assumption breaks down, which will negatively affect the accuracy of this method.

3. Method

The missing derivatives of the lattice distortion, $\beta_{ij,3}$, mean that only the α_{i3} terms are known for certain, and only when calculated in a reference frame where the z-axis is normal to the sample surface. This in turn prevents rotating α into the detector frame, where the noisy components on the distortion derivatives are isolated into individual terms. Instead, the noisy terms in the derivative must be dealt with in the detector reference frame before rotating into the sample frame and taking the curl. The method presented here for minimizing the contribution of the noisy distortion terms on the determination of dislocation density is referred to as enforced antisymmetry. This method involves sacrificing some amount of information to reduce the effects of noise on dislocation density calculations.

For this method, the relative elastic distortions between points are rotated into the reference frame of the detector and the problematic terms, β_{31} and β_{32}, are discarded and replaced by -β_{13} and -β_{23}, respectively. This substitution is appropriate only when the relative distortion is expected to be approximately antisymmetric, as is

the case when the distortion is small, strain free rotation. The strain free assumption is already made in the development of Nye's tensor and in Pantleon's assumption to recover more of the missing terms of Nye's tensor. The relationship between noise in measuring dislocation shifts and terms of β (Equations 4-8) suggest that making this change reduces the operator 2-norm of the noise by a factor of 2.8 for a typical HREBSD set up. This comes at the expense of some bias error associated with the neglected symmetric part of the discarded and replicated terms. Other attempts to neglect strain effects, such as averaging the β_{12} and -β_{21} terms, using only the antisymmetric part of β (ω) and/or performing polar decomposition after enforcing antisymmetry to enforce a pure rotation, led to a discrepancy between the HREBSD-based GND measurements and the ECCI- and TEM-based measurements in terms of the predicted dislocation system, presumably because the strain portion of the derivatives is critical. This result suggests that strain free assumptions (like Pantleon's assumption and the enforced antisymmetry presented here) introduce error into Nye-Kröner analysis at small length scales. Despite this potential source of error, qualitative agreement is still achieved between HREBSD dislocation microscopy and ECCI and TEM. In order to preserve as much strain information as possible, only the noisiest two terms are discarded. Once this antisymmetry constraint is enforced, the relative distortion terms may be rotated back into the sample frame, the derivatives may be determined using Equation 9, and the whole algorithm proceeds as expected. In practical terms, the strains tend to be a small part of the relative distortion when step sizes are large because a large number of dislocations will tend to arrange themselves in a way that minimizes residual elastic energy, i.e. strain. However, when step sizes and dislocation densities are lower, as in the case when there is an attempt to locate single dislocations, this, and other strain free assumptions may introduce error.

This method was tested on a scan taken from a region on a stainless steel sample after first characterizing the dislocation content via TEM. The type 302 stainless steel sheet was purchased from VWR (Catalog No. 300082-552). A 2×2 cm square piece was cut out with wire electrical discharge machining (EDM) and annealed at 1060°C for 30 minutes in a reducing atmosphere of N_2 and H_2 mixture. The annealed sample was then thinned using Struers Rotopol-15 and a 3 mm disk was prepared using a punch-out. The disk was then jet polished using Fischione Model 110 Automatic Twin-Jet Electropolisher using a 10% perchloric acid and 90% ethanol solution at -25°C. Electron micrographs were collected using a FEI Tecnai F30 TEM at 300 kV acceleration voltage. EBSD patterns were collected using a TESCAN MIRA3 SEM equipped with an EDAX/TSL Hikari highspeed detector. The accelerating voltage was 20 kV and the sample was tilted to a conventional 70°. All EBSD patterns were saved at 1×1 binning (465×465 pixels) for offline analysis. The HREBSD calculations were carried out using OpenXY, an open source software package, with modifications to implement the noise reducing methods mentioned [59]. The 48 ROIs were sized to be 25% of the detector width, and they were arranged annularly. Distortion derivatives were determined by comparing neighboring points, which kept relative distortion terms below $1000\mu\varepsilon$. In addition to the noise reduction method discussed, a local average was performed on the distortion derivatives to smooth the data and eliminate some of the noise at the expense of spatial resolution. Individual dislocation densities were determined using all 6 of Pantleon's constraints.

The noise reduction method was also tested on an HREBSD scan around a nanoindent in a tantalum oligocrystal. The area scanned was first characterized via ECCI analysis. For details concerning the preparation, HREBSD scan parameters and ECCI analysis of the tantalum sample examined in this study, please refer to previous work by the authors [27].

4. Results

The grain containing the pile-ups was determined to have a crystallographic orientation defined by the Euler-Bunge angles $[85.6^o, 39.9^o, 287.5^o]$, which corresponds to a surface plane normal aligned with the $[\bar{3}14]$ crystallographic direction. Figure 3 shows bright field TEM images of the area of interest in two different diffraction conditions: $\vec{g} = 111$ (Figure 3a) and $\vec{g} = 02\bar{2}$ (Figure 3b). The first pile-up of interest, labeled system 1, is the most prominent pile-up under the diffraction condition $g = 111$, but it is invisible under $g = 02\bar{2}$, indicating that the Burgers vector of the dislocation system is $\vec{b} = a/2[011]$, where a is the lattice parameter. The second pile-up, labeled system 2, cuts across the first pile-up and is clearly visible under $\vec{g} = 02\bar{2}$ but is seen only edge-on under $\vec{g} = 111$, indicating that these dislocations lie on the (111) plane. Additional diffraction analysis identified the system 1 slip plane and the dislocation line direction as $(\bar{1}1\bar{1})$ and $[011]$ respectively and the system 2 dislocations as having a Burgers vector of $\vec{b} = a/2[0\bar{1}1]$. Multiple secondary phase particles with dislocations accumulated around them are

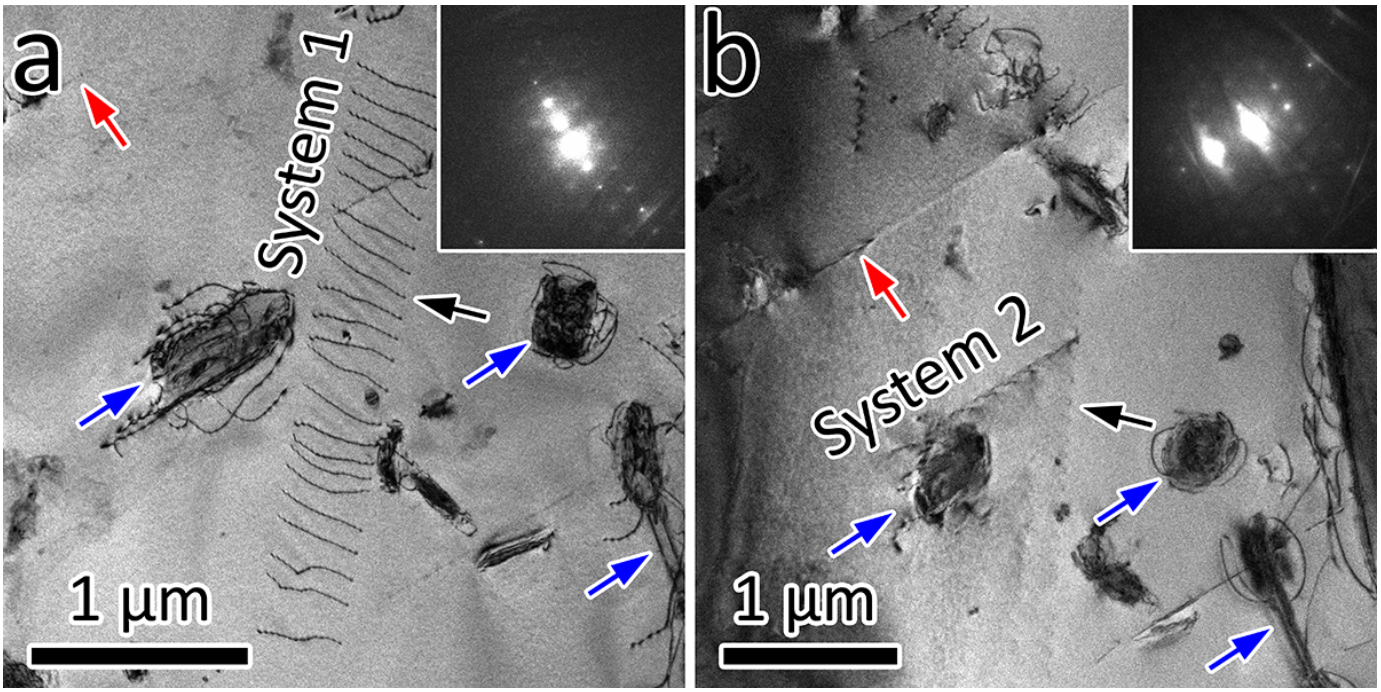

Figure 3: Bright field TEM images of the dislocation pileups of interest from two different diffracting conditions: $g = 111$ (a) and $g = 02\bar{2}$ (b). Red arrows indicate the twin boundary, blue arrows denote the fiducial secondary phase particles, and the black arrows indicate a common point on the system 1 pile-up.

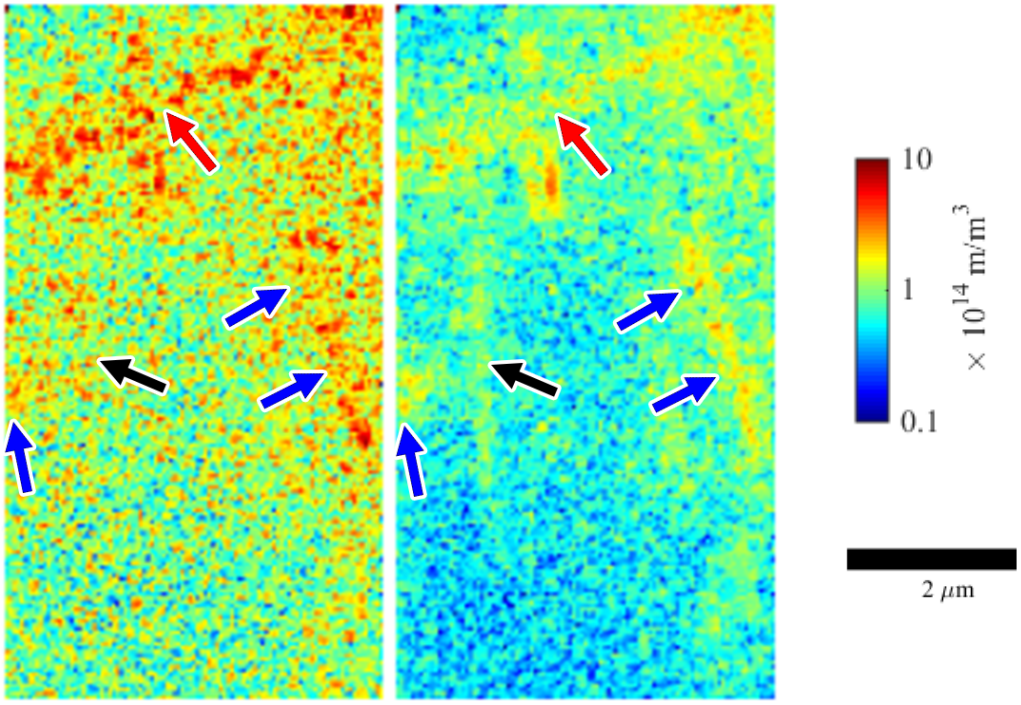

(a) (b)

Figure 4: Log plot of the total dislocation density of the region of interest as determined by HREBSD without (a) and with (b) enforced antisymmetry noise reduction.

visible in the image (Figure 3 blue arrows), as well as a twin boundary (indicated by a red arrow). These features facilitated direct alignment with the HREBSD scan.

The relative distortion (β) between each point and its neighbor to the right and to the top are mapped in Figures 6 and 5 respectively. These relative distortions, used to

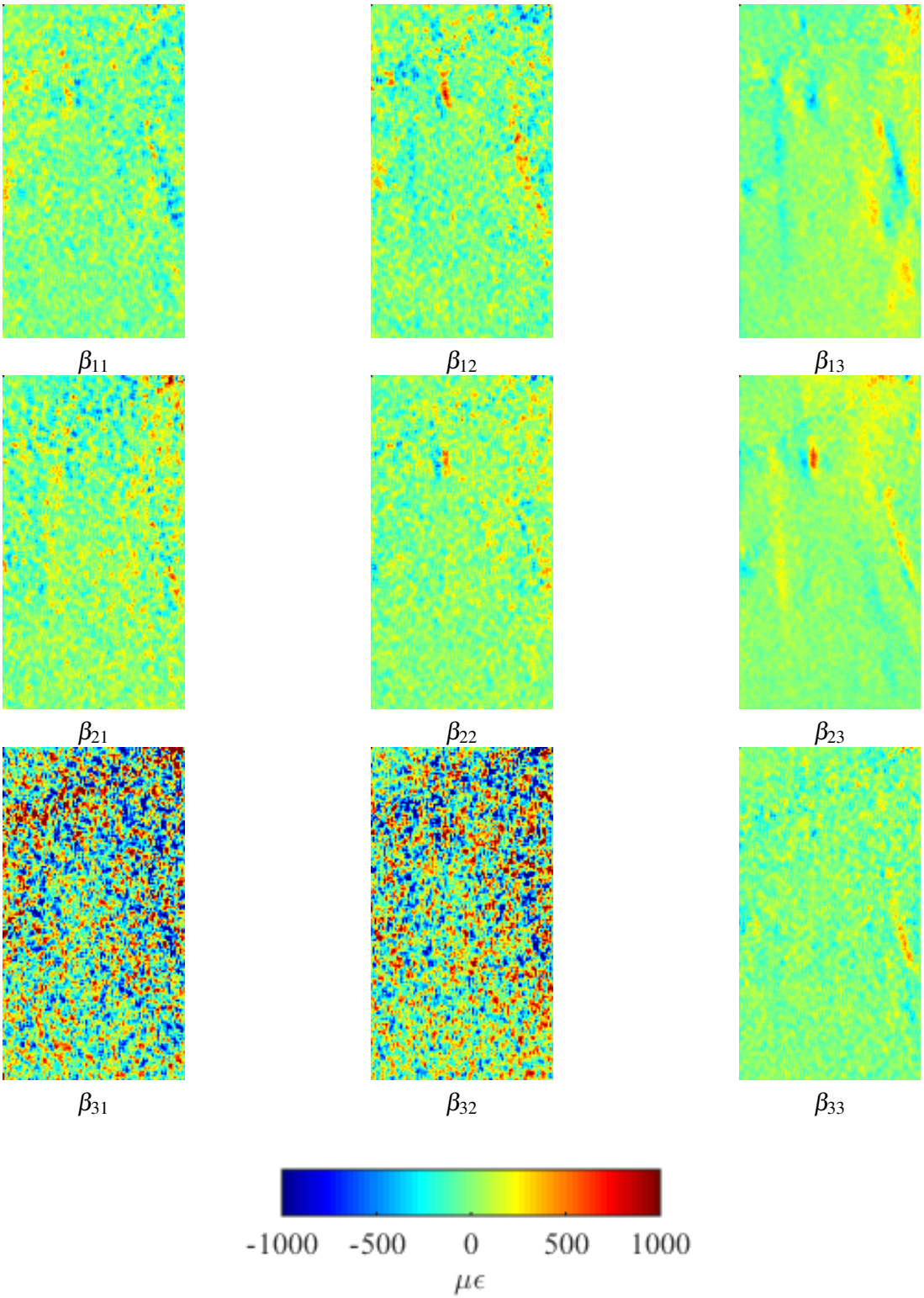

Figure 5: Relative distortion measured via cross-correlation between each point and its neighbor to the right. Distortions are in the reference frame of the detector screen, where the $\hat{z}$-axis is normal to the detector surface

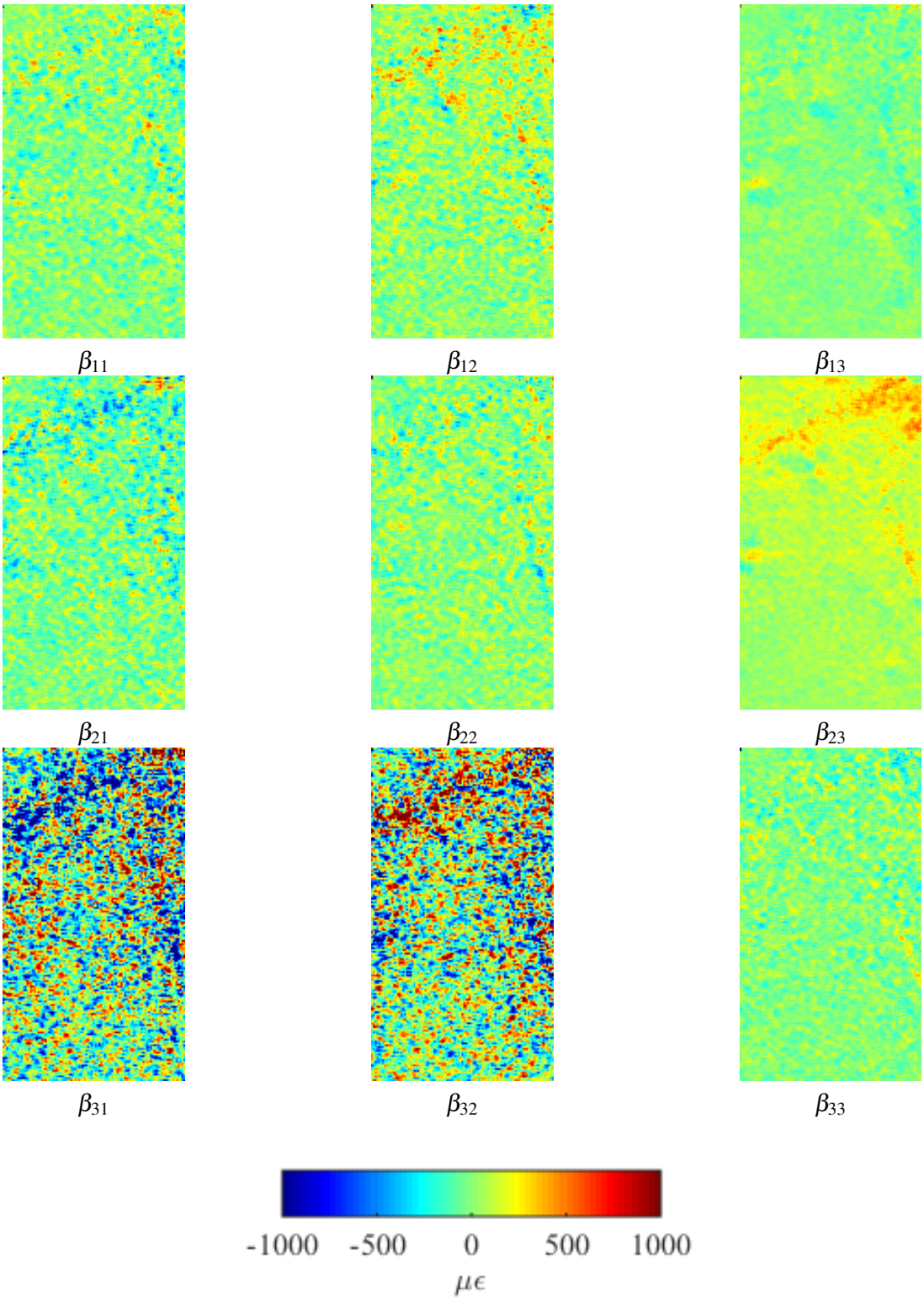

Figure 6: Relative distortion measured via cross-correlation between each point and its neighbor to the top. Distortions are in the reference frame of the detector screen, where the $\hat{z}$-axis is normal to the detector surface

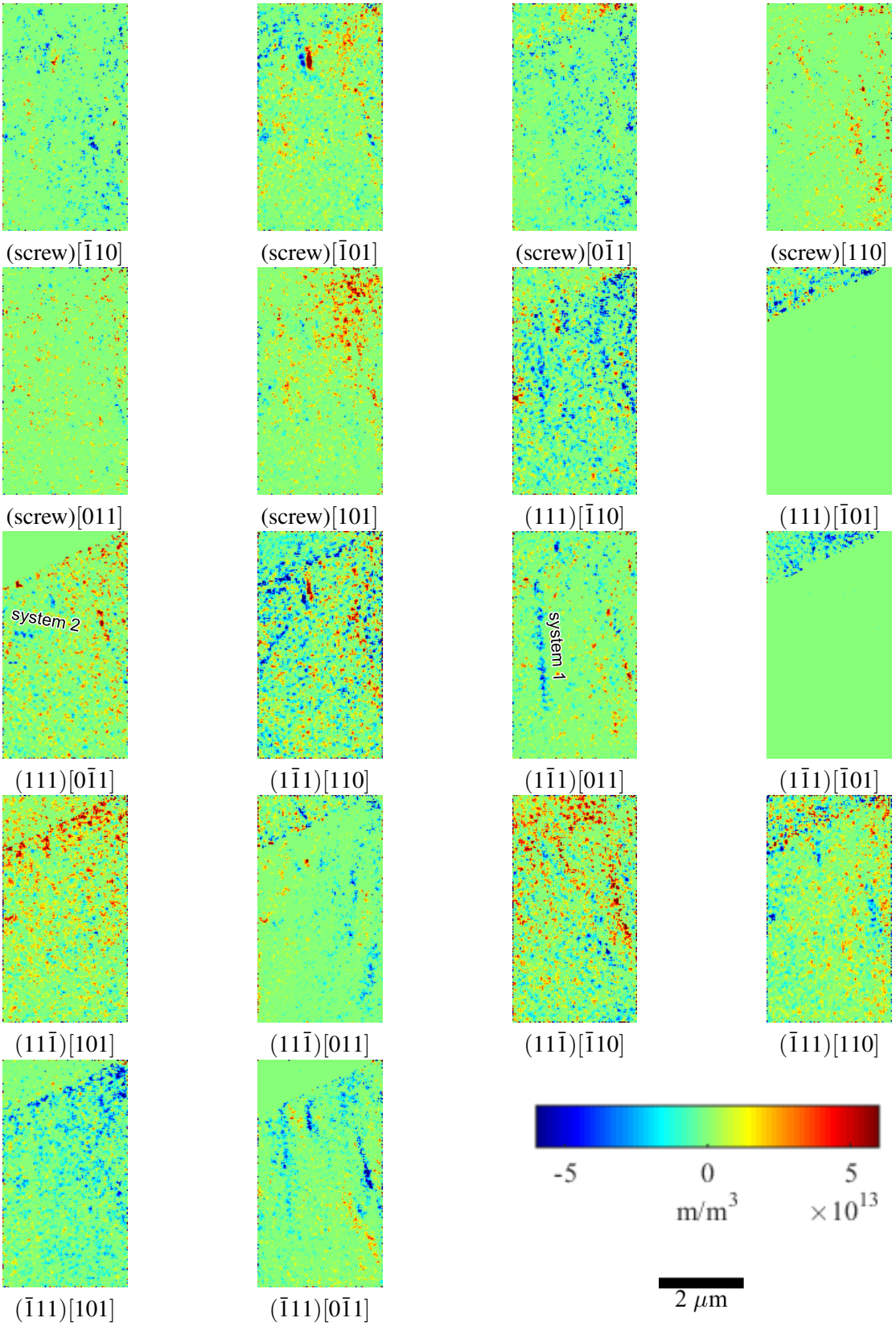

Figure 7: Dislocation density measured by HREBSD resolved onto individual dislocation types according to Equation 12 in austenitic stainless steel. Negative densities represent dislocation density with an opposite signed Burgers vector.

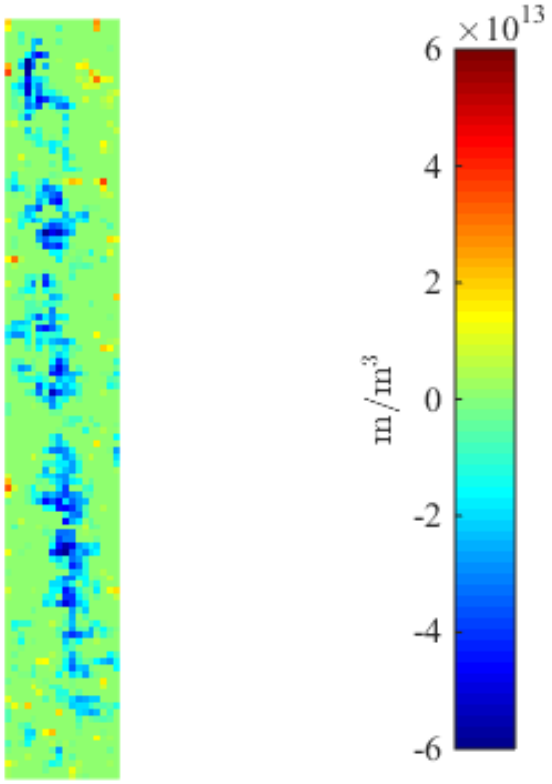

Figure 8: A detail of the dislocation density map for the $[011](1\bar{1}1)$ edge dislocation that shows only the dislocation pile-up on system 1 shown in Figures 3-7.

calculate distortion derivatives, have been smoothed to reduce noise. They are presented in the reference frame of the detector so that the noisy β_{31} and β_{32} terms are apparent. These terms are removed and replaced with $-\beta_{13}$ and $-\beta_{23}$ respectively before being rotated into the sample reference frame and used to calculate derivatives. The total calculated dislocation density (with derivative smoothing and all 6 of Pantleon's constraints) from the HREBSD scan of the same area is shown in Figure 4 with and without enforced antisymmetry noise reduction. While the fiducial features marked in the TEM micrograph are difficult to distinguish without noise reduction, they are visible with noise reduction enabled. All of the same features are highlighted. Note that because the interaction volume of EBSD is only a few nanometers deep, the dislocation pile-up appears as a line where the dislocations intersect the surface of the material.

The HREBSD results for the dislocation density of each type, as determined by Equation 12, are shown in Figure 7. Negative values represent dislocation densities with Burgers vectors that have the opposite sign. The absolute value of these densities was summed to generate Figure 4b. System 1 is identified as edge dislocations with Burgers vector $\vec{b} = a/2[011]$ on the $(1\bar{1}1)$ slip plane. System 2 is identified as edge dislocations with Burgers vector $\vec{b} = a/2[0\bar{1}1]$ on the (111) plane. That is, in both cases the dislocation Burgers vector was correctly identified, but the slip plane and dislocation type were only identified correctly in system 2. The trace of system 2 with the free surface deviates in the two measurements, suggesting potential local charging effects near the second phase particle during HREBSD pattern acquisition. One possible cause of this misidentification in system 1 is that the information lost when enforcing antisymmetry or applying Pantelon's assumption (both of which involve neglecting strain) affects the resolution of the dislocation density onto individual slip systems. Note that while the underconstrained nature of Equation 12 and the arbitrary inclusion of the energy minimization constraint can lead to misidentification, simulations suggest that at this grain's orientation under ideal circumstances and including Pantleon's extra constraints, these two dislocations should be readily resolved. When only the α_{i3} terms are considered, distinguishing between the $[011](1\bar{1}1)$ edge dislocation and the $[011]$ screw dislocation becomes ambiguous. An alternative explanation is that image forces lead to a change in dislocation line direction where the dislocation intersects the free surface. Image forces most strongly affect dislocations that lie parallel to the free surface, causing the dislocation segments near the free surface to bend towards the surface. In the characterized dislocation systems, TEM analysis showed that the system 2 dislocations lie near-perpendicular to the surface normal while the system 1 dislocation line direction is near parallel to the free surface, supporting the image force hypothesis for the dislocation misidentification.

In addition to the identified dislocation systems, there are regions of high local dislocation density. Some of these can clearly be attributed to dislocations surrounding second phase particles, such as the $(\bar{1}11)[0\bar{1}1]$ system seen in Figure 7, but there is also a large amount of dislocation density noise for certain dislocation types. Because the noise has varying magnitude in each term of the measured distortion (even after enforced antisymmetry), phantom dislocation identification can still occur in the measurements.

The dislocation densities measured are all well below the threshold of one dislocation per pixel. This occurs because a single dislocation is not detected as a point defect where it intersects with the surface, but instead as a diffuse distortion field. The diffuse nature of these dislocation densities is due to both the smoothing operation and the finite size of the EBSD interaction volume, as well as

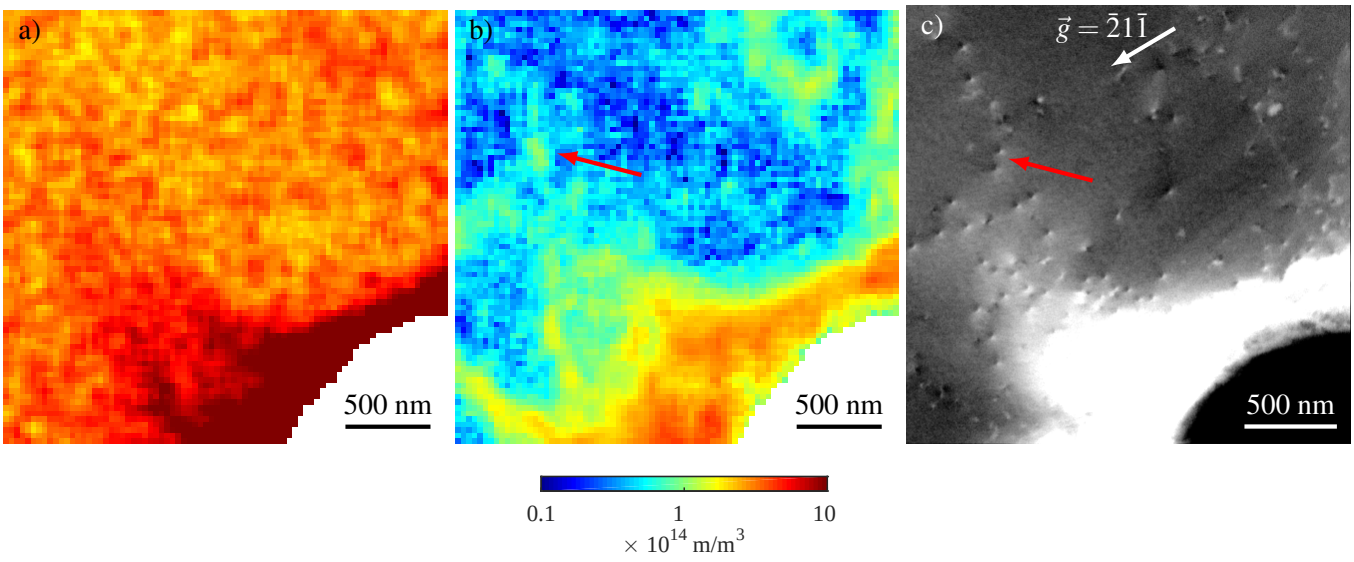

Figure 9: Three different images of the dislocation content around a nanoindent in tantalum: Log plot HREBSD total dislocation density without (a) and with (b) noise reduction as well as an ECCI image (c). Images (a) and (c) are from a previous study by the authors [27]. A red arrow marks a dislocation pair as an example of a feature visible in both forms of imaging. In (a) and (b), points with a confidence index below .18 are whited out to exclude the indent and material too damaged or out-of-plane for successful HREBSD.

the fact that the distortion fields around a single dislocation are detectable for at least 100 nm. To emphasize this effect, a detail of the $[011](1\bar{1}1)$ dislocation density map (as seen in Figure 7) which corresponds to the system 1 pile-up in Figure 3 is shown in Figure 8. Summing the density at each point in this subsection of the $[011](1\bar{1}1)$ dislocation density map and multiplying by the area results in a value of only 8.8 dislocations, whereas the TEM micrograph (Figure 3) suggests that there are actually 23 dislocations intersecting the surface. This discrepancy is most likely due to one or more of the following factors: the effect of a finite interaction volume, step size effects on derivative measurements and the fact that the algorithm neglects strain (both when applying Pantleon's assumption and when applying noise reduction). The influence of these factors should decrease with larger EBSD step sizes. However, when viewed at this higher magnification, it becomes obvious that individual dislocations, which appear diffuse and equi-axed, have been identified. It is more difficult to resolve individual dislocations when the dislocation spacing is smaller. Counting the dislocations by hand in the $(1\bar{1}1)[011]$ dislocation density map yields around 20 dislocations, although this method is somewhat subjective and laborious. Note that if all other dislocation types are taken into account, many of which are preferentially affected by noise, 91.1 dislocations are detected in this area, which is consistent with the high background noise. If the actual dislocation type were one of the phantom noise dislocations, detecting it would be less likely.

The noise reduction technique was also applied to an EBSD scan collected near a nano-indentation in a tantalum oligocrystal. This scan was used in a previous work by the authors where ECCI analysis was also performed on the same area and the results were compared [27]. In the previous study, there was good general agreement, but correlating individual dislocations was impossible. After the application of noise reduction, however, features, including individual dislocations, are much easier to correlate. The total dislocation density as determined via HREBSD with and without noise reduction is contrasted with the ECCI image of the dislocation structure in Figure 9. Agreement is now much more obvious, and individual dislocations may be directly correlated between the ECCI and the HREBSD data. In the previous study, the majority of the individually distinguishable dislocations in the upper left quadrant of the ECCI micrograph were found to be screw dislocations with a Burgers vector of $[111]$. This is confirmed by plotting the individual dislocation densities in Figure 10. A red arrow marks one dislocation pair in Figures 9 and 10.

5. Conclusion

In this study, HREBSD dislocation density measurements were compared with TEM characterization of two dislocation pile-ups near a twin boundary in austenitic stainless steel. To make this comparison possible, the

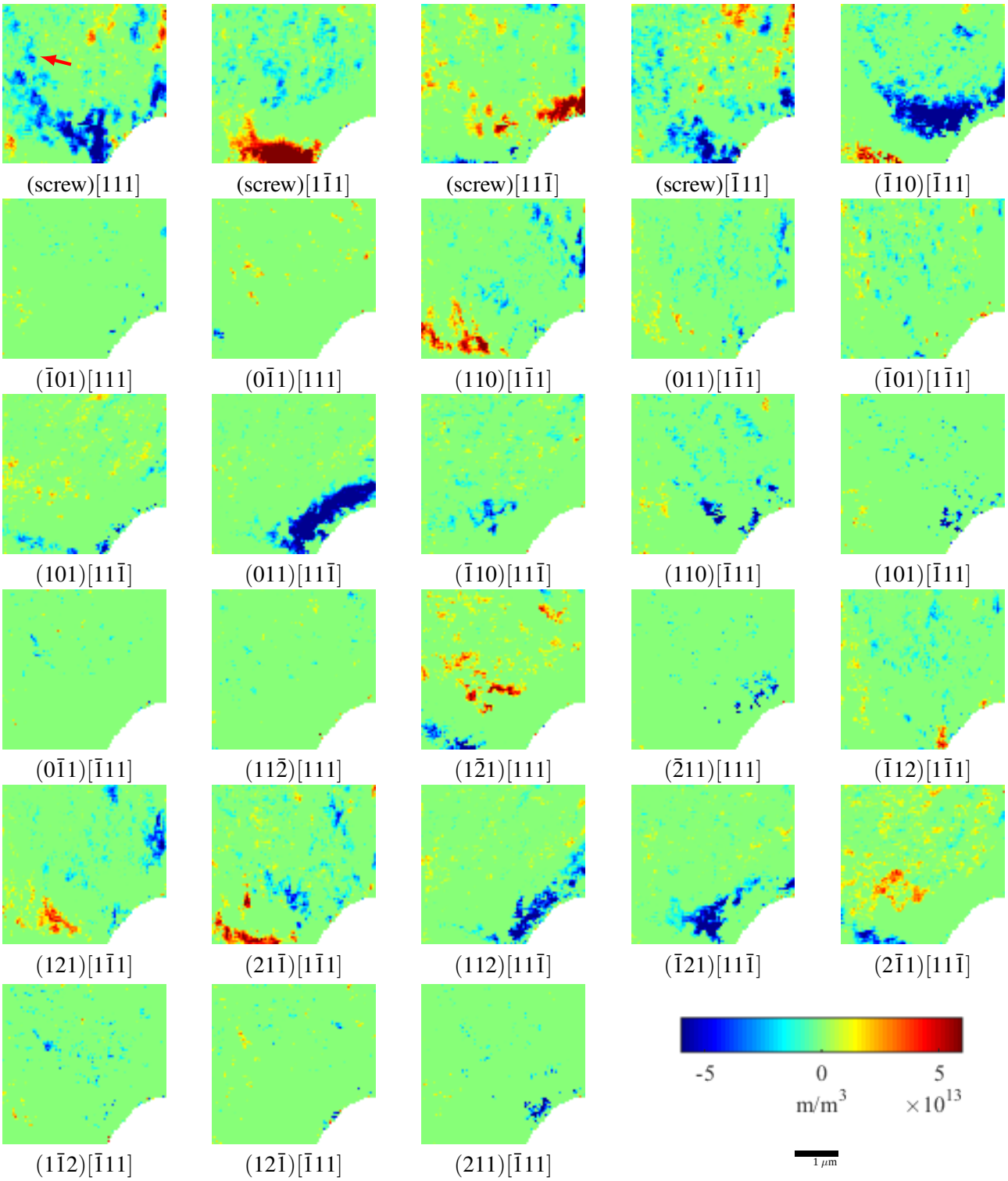

Figure 10: Dislocation density measured by HREBSD resolved onto individual dislocation types according to Equation 12 near a nanoindent in tantalum. Negative densities represent dislocation density with an opposite signed Burgers vector. A red arrow marks the dislocation pair also marked in Figure 9.

noise in the HREBSD measurements was reduced by discarding problematic terms of the measured lattice distortion in the detector reference frame. The two methods showed good qualitative agreement as to the location and distribution of the dislocations. HREBSD dislocation microscopy successfully identified the Burgers vector of the dislocations in the pile-ups, but only identified the slip plane in one of the two systems. It is thought that this is due to image forces locally changing the dislocation line direction.

Quantitatively, the predicted densities were low by a factor of around three compared to the TEM analysis, most likely due to the effect of finite interaction volume of EBSD, local smoothing done to reduce noise and the fact that strain was neglected. Additionally, noise in the dislocation density measurements, which manifests as predictions of dislocation density on other, erroneous slip systems, were still of a comparatively high magnitude even with the noise reduction technique. However, use of the $[011](1\bar{1}1)$ dislocation density map to count individual dislocations yields a more accurate, if crude, estimate of the actual dislocation content of the material. Considering that the Nye-Kröner-Bilby method of relating lattice distortion to geometrically necessary dislocation content was originally intended to be employed at the continuum scale, this level of agreement is impressive. Additionally, it is necessary to assume that strain is negligible at a number of steps in this technique (Nye-Kröner, Pantleon, and the assumption made here to perform denoising), which is not the case at low length scales. This will negatively impact both quantitative and in some cases qualitative agreement. To mitigate these issues, future efforts to use HREBSD/TKD to detect individual dislocations should be formulated to address the discrete nature of dislocations, the finite interaction volume size, the presence of strain at low length scales and the uncertainty in measuring the lattice distortion gradients. These efforts will likely rely on forward modeling of the distortion fields around dislocations and uncertainty quantification to accommodate the noise.

The noise reduction technique for HREBSD was also compared with ECCI characterization of the dislocation content around a nanoindent in a tantalum oligocrystal. Both methods successfully identified the dislocations in the area of interest as screw dislocations with a Burgers vector of $[111]$ showing that the improved resolution demonstrated in the austenitic stainless steel is not limited to thin specimens or FCC crystal structures. The ability to resolve individual defects with EBSD is likely to continue improving as EBSD hardware and HREBSD methods continue to develop in terms of both spatial and strain resolution.

Acknowledgments

TEM imaging and analysis by YSJY and JK were supported by the U.S. Department of Energy (DOE), Office of Science, Basic Energy Sciences (BES) Materials Science and Engineering (MSE) Division under award #DE-SC0018960.

BED and MAC were supported by the US Department of Energy through grant #DE-FG02-09ER46637. The tantalum used in this study was provided by Sandia National Laboratories.

Data Availability

The data collected for this study is free to share. Please contact the authors for access.

References

[1] M. A. Crimp, Scanning electron microscopy imaging of dislocations in bulk materials, using electron channeling contrast, Microscopy research and technique 69 (5) (2006) 374–381.

[2] S. Zaefferer, N.-N. Elhami, Theory and application of electron channelling contrast imaging under controlled diffraction conditions, Acta Materialia 75 (2014) 20–50.

[3] M. Crimp, B. Simkin, B. Ng, Demonstration of the $\mathbf{g}\cdot\mathbf{b}\times\mathbf{u}=\mathbf{0}$ edge dislocation invisibility criterion for electron channelling contrast imaging, Philosophical Magazine Letters 81 (12) (2001) 833–837.

[4] H. Mansour, J. Guyon, M. Crimp, N. Gey, B. Beausir, N. Maloufi, Accurate electron channeling contrast analysis of dislocations in fine grained bulk materials, Scripta Materialia 84 (2014) 11–14.

[5] M. Pitaval, P. Morin, J. Baudry, E. Vicario, G. Fontaine, Advances in crystalline contrast from defects, Scanning Electron Microscopy (1977) 439–444.

[6] S. I. Wright, M. M. Nowell, R. de Kloe, L. Chan, Orientation precision of electron backscatter diffraction measurements near grain boundaries, Microscopy and Microanalysis 20 (2014) 852–863.

[7] F. Ram, S. Zaefferer, T. Jäpel, D. Raabe, Error analysis of the crystal orientations and disorientations obtained by the classical electron backscatter diffraction technique, Journal of Applied Crystallography 48 (3) (2015) 797–813.

[8] B. L. Adams, Orientation imaging microscopy: Emerging and future applications, Ultramicroscopy 67 (1-4) (1997) 11–17.

[9] S. Sun, B. Adams, W. King, Observations of lattice curvature near the interface of a deformed aluminium bicrystal, Philosophical Magazine A: Physics of Condensed Matter, Structure, Defects and Mechanical Properties 80 (1) (2000) 9–25.

[10] J. Kysar, Y. Saito, M. Oztop, D. Lee, W. Huh, Experimental lower bounds on geometrically necessary dislocation density, International Journal of Plasticity 26 (2010) 1097–1123.

[11] P. Konijnenberg, S. Zaefferer, D. Raabe, Assessment of geometrically necessary dislocation levels derived by 3D EBSD, Acta Materialia 99 (2015) 402 – 414.

[12] A. J. Wilkinson, G. Meaden, D. J. Dingley, High resolution mapping of strains and rotations using electron back scatter diffraction, Materials Science and Technology 22 (11) (2006) 1–11.

[13] C. J. Gardner, B. L. Adams, J. Basinger, D. T. Fullwood, EBSD-based continuum dislocation microscopy, International Journal of Plasticity 26 (2010) 1234–1247.

[14] T. Britton, H. Liang, F. Dunne, A. Wilkinson, The effect of crystal orientation on the indentation response of commercially pure titanium: experiments and simulations, Proceedings of the Royal Society of London A: Mathematical, Physical and Engineering Sciences 466 (2115) (2010) 695–719.

[15] T. B. Britton, A. J. Wilkinson, Stress fields and geometrically necessary dislocation density distributions near the head of a blocked slip band, Acta Materialia 60 (16) (2012) 5773 – 5782.

[16] A. Wilkinson, D. Randman, Determination of elastic strain fields and geometrically necessary dislocation distributions near nanoindents using electron back scatter diffraction, Philosophical Magazine 90 (9) (2010) 1159–1177.

[17] T. J. Ruggles, D. T. Fullwood, Estimations of bulk geometrically necessary dislocation density using high resolution EBSD, Ultramicroscopy 133 (2013) 8–15.

[18] J. Jiang, T. B. Britton, A. J. Wilkinson, The orientation and strain dependence of dislocation structure evolution in monotonically deformed polycrystalline copper, International Journal of Plasticity 69 (2015) 102–117.

[19] T. Ruggles, D. Fullwood, J. Kysar, Resolving geometrically necessary dislocation density onto individual dislocation types using EBSD-based continuum dislocation microscopy, International Journal of Plasticity 76 (2016) 231 – 243.

[20] S. R. Yeratapally, J. D. Hochhalter, T. J. Ruggles, M. D. Sangid, Investigation of fatigue crack incubation and growth in cast MAR-M247 subjected to low cycle fatigue at room temperature, International Journal of Fracture 208 (2017) 79–96.

[21] S. Kalácska, I. Groma, A. Borbély, P. D. Ispánovity, Comparison of the dislocation density obtained by HR-EBSD and X-ray profile analysis, Applied Physics Letters 110 (9) (2017) 091912.

[22] D. Wallis, A. J. Parsons, L. N. Hansen, Quantifying geometrically necessary dislocations in quartz using HR-EBSD: Application to chessboard subgrain boundaries, Journal of Structural Geology 125 (2017) 235 – 247.

[23] F. Javaid, E. Bruder, K. Durst, Indentation size effect and dislocation structure evolution in (001) oriented $SrTiO_3$ Berkovich indentations: HR-EBSD and etch-pit analysis, Acta Materialia 139 (2017) 1 – 10.

[24] C. Zhao, D. Stewart, J. Jiang, F. P. Dunne, A comparative assessment of iron and cobalt-based hard-facing alloy deformation using HR-EBSD and HR-DIC, Acta Materialia 159 (2018) 173 – 186.

[25] F. Ram, Z. Li, S. Zaefferer, S. M. H. Haghighat, Z. Zhu, D. Raabe, R. C. Reed, On the origin of creep dislocations in a Ni-base, single-crystal superalloy: an ECCI, EBSD, and dislocation dynamics-based study, Acta Materialia 109 (2016) 151 – 161.

[26] A. Vilalta-Clemente, G. Naresh-Kumar, M. Nouf-Allehiani, P. Gamarra, M. di Forte-Poisson, C. Trager-Cowan, A. Wilkinson, Cross-correlation based high resolution electron backscatter diffraction and electron channelling contrast imaging for strain mapping and dislocation distributions in InAlN thin films, Acta Materialia 125 (2017) 125 – 135.

[27] B. E. Dunlap, T. J. Ruggles, D. T. Fullwood, B. Jackson, M. A. Crimp, Comparison of dislocation characterization by electron channeling contrast imaging and cross-correlation electron backscattered diffraction, Ultramicroscopy 184 (2018) 125 – 133.

[28] Y. S. J. Yoo, T. A. Book, M. D. Sangid, J. Kacher, Identifying strain localization and dislocation processes in fatigued Inconel 718 manufactured from selective laser melting, Materials Science and Engineering: A 724 (2018) 444 – 451.

[29] P. W. Trimby, Orientation mapping of nanostructured materials using transmission Kikuchi diffraction in the scanning electron microscope, Ultramicroscopy 120 (2012) 16 – 24.

[30] R. Keller, R. Geiss, Transmission EBSD from 10 nm domains in a scanning electron microscope, Journal of Microscopy 245 (3) (2012) 245–251.

[31] J. Kacher, P. Elizaga, S. D. House, K. Hattar, M. Nowell, I. Robertson, Thermal stability of Ni/NiO multilayers, Materials Science and Engineering: A 568 (2013) 49 – 60.

[32] A. J. Wilkinson, G. Moldovan, T. B. Britton, A. Bewick, R. Clough, A. I. Kirkland, Direct detection of electron backscatter diffraction patterns, Phys. Rev. Lett. 111 (2013) 065506.

[33] F. Ram, S. Wright, S. Singh, M. D. Graef, Error analysis of the crystal orientations obtained by the dictionary approach to EBSD indexing, Ultramicroscopy 181 (2017) 17 – 26.

[34] G. Nolze, M. Jürgens, J. Olbricht, A. Winkelmann, Improving the precision of orientation measurements from technical materials via EBSD pattern matching, Acta Materialia 159 (2018) 408 – 415.

[35] B. Jackson, D. Fullwood, J. Christensen, S. Wright, Resolving pseudosymmetry in γ-TiAl using cross-correlation electron backscatter diffraction with dynamically simulated reference patterns, Journal of Applied Crystallography 51 (3) (2018) 655–669.

[36] X. Liang, M. Dodge, J. Jiang, H. Dong, Using transmission Kikuchi diffraction in a scanning electron microscope to quantify geometrically necessary dislocation density at the nanoscale, Ultramicroscopy 197 (2019) 39 – 45.

[37] H. Yu, J. Liu, P. Karamched, A. J. Wilkinson, F. Hofmann, Mapping the full lattice strain tensor of a single dislocation by high angular resolution transmission Kikuchi diffraction (HR-TKD), arXiv e-prints (2018) arXiv:1808.10055arXiv:1808.10055.

[38] J. Alkorta, Limits of simulation based high resolution EBSD, Ultramicroscopy 131 (2013) 33–38.

[39] T. J. Ruggles, G. F. Bomarito, A. H. Cannon, J. D. Hochhalter, Selectively electron-transparent microstamping toward concurrent digital image correlation and high-angular resolution electron backscatter diffraction (EBSD) analysis, Microscopy and Microanalysis 23 (6) (2017) 1091 – 1095.

[40] T. Vermeij, J. Hoefnagels, A consistent full-field integrated DIC framework for HR-EBSD, Ultramicroscopy 191 (2018) 44 – 50.

[41] T. Ruggles, G. Bomarito, R. Qiu, J. Hochhalter, New levels of high angular resolution EBSD performance via inverse compositional Gauss–Newton based digital image correlation, Ultramicroscopy 195 (2018) 85 – 92.

[42] T. Vermeij, M. D. Graef, J. Hoefnagels, Demonstrating the potential of accurate absolute cross-grain stress and orientation correlation using electron backscatter diffraction, Scripta Materialia 162 (2019) 266 – 271.

[43] Q. Shi, S. Roux, F. Latourte, F. Hild, Estimation of elastic strain by integrated image correlation on electron diffraction patterns, Ultramicroscopy 199 (2019) 16 – 33.

[44] T. Hardin, T. Ruggles, D. Koch, S. Niezgoda, D. Full-

wood, E. Homer, Analysis of traction-free assumption in high-resolution EBSD measurements, Journal of Microscopy (2015).
[45] C. Maurice, J. H. Driver, R. Fortunier, On solving the orientation gradient dependency of high angular resolution EBSD, Ultramicroscopy 113 (2012) 171–181.
[46] T. Britton, J. Jiang, R. Clough, E. Tarleton, A. Kirkland, A. Wilkinson, Assessing the precision of strain measurements using electron backscatter diffraction – part 1: Detector assessment, Ultramicroscopy 135 (2013) 126 – 135.
[47] L. T. Hansen, B. E. Jackson, D. T. Fullwood, S. I. Wright, M. De Graef, E. R. Homer, R. H. Wagoner, Influence of noise-generating factors on cross-correlation electron backscatter diffraction (EBSD) measurement of geometrically necessary dislocations (GNDs), Microscopy & Microanalysis 23 (3) (2017) 460–471.
[48] T. Britton, A. Wilkinson, High resolution electron backscatter diffraction measurements of elastic strain variations in the presence of larger rotations, Ultramicroscopy 114 (2012) 82–95.
[49] E. Kröner, Continuum theory of dislocations and self-stresses, Ergebnisse der Angewandten Mathematik 5 (1958) 1327–1347.
[50] E. Kröner, Modified green functions in the theory of heterogeneous and/or anisotropic linearly elastic media, in: G. Weng, M. Abe (Eds.), Micromechanics and Inhomogeneity, Springer, Berlin, 1989, pp. 197–211.
[51] B. Bilby, L. Gardner, E. Smith, The relation between dislocation density and stress, Acta Metallurgica 6 (1) (1958) 29 – 33.
[52] J. Nye, Some geometrical relations in dislocated crystals, Acta Metallurgica 1 (1953) 153–162.
[53] W. Pantleon, Resolving the geometrically necessary dislocation content by conventional electron backscattering diffraction, Scripta Materialia 58 (11) (2008) 994 – 997.
[54] D. Field, C. Merriman, J. Smith, Excess dislocation density measurement dependence on EBSD step size, Microscopy & Microanalysis 13 (2007) 920–921.
[55] B. Adams, J. Kacher, EBSD-based microscopy: Resolution of dislocation density, Computers, Materials and Continua 14 (3) (2010) 185–196.
[56] J. Jiang, T. Britton, A. Wilkinson, Measurement of geometrically necessary dislocation density with high resolution electron backscatter diffraction: Effects of detector binning and step size, Ultramicroscopy 125 (2013) 1–9.
[57] A. Leff, C. Weinberger, M. Taheri, Estimation of dislocation density from precession electron diffraction data using the Nye tensor, Ultramicroscopy 153 (0) (2015) 9 – 21.
[58] T. Ruggles, T. Rampton, A. Khosravani, D. Fullwood, The effect of length scale on the determination of geometrically necessary dislocations via EBSD continuum dislocation microscopy, Ultramicroscopy 164 (2016) 1 – 10.
[59] Brigham Young University, OpenXY (2016).